POLITECNICO DI TORINO
Repository ISTITUZIONALE

Wide and tunable spectral asymmetry between narrow and wide facet outputs in a tapered quantum-dot superluminescent diode

Original
Wide and tunable spectral asymmetry between narrow and wide facet outputs in a tapered quantum-dot superluminescent diode / Forrest, A. F.; Krakowski, M.; Bardella, P.; Cataluna, M. A.. - In: OPTICS EXPRESS. - ISSN 1094-4087. - ELETTRONICO. - 28:2(2020), pp. 846-859. [10.1364/OE.377768]

Availability:
This version is available at: 11583/2795848 since: 2020-02-20T19:25:24Z

Publisher:
OSA - The Optical Society

Published
DOI:10.1364/OE.377768

Terms of use:

This article is made available under terms and conditions as specified in the corresponding bibliographic description in the repository

Publisher copyright

(Article begins on next page)

27 September 2024

Research Article Vol. 28, No. 2 / 20 January 2020 / Optics Express 846

Optics EXPRESS

Wide and tunable spectral asymmetry between narrow and wide facet outputs in a tapered quantum-dot superluminescent diode

ADAM F. FORREST,[1,2,*] MICHEL KRAKOWSKI,[3] PAOLO BARDELLA,[4] AND MARIA ANA CATALUNA[1,2]

[1] *Institute of Photonics and Quantum Science, School of Engineering and Physical Sciences, Heriot-Watt University, Edinburgh Campus, Edinburgh, EH14 4AS, United Kingdom*
[2] *Previously also with the School of Science and Engineering, University of Dundee, Dundee, DD1 4HN, United Kingdom*
[3] *III-V Lab, 1 Avenue Augustin Fresnel, Campus de Polytechnique, 91767 Palaiseau, France*
[4] *Dipartimento di Elettronica e Telecomunicazioni, Politecnico di Torino, I-10129, Turin, Italy*
[*] *adam.forrest@hw.ac.uk*

Abstract: A wide spectral asymmetry between the front and rear facets of a tapered chirped quantum dot multi-section superluminescent diode is reported. The spectral asymmetry between the two facet outputs was found to be tunable and highly dependent on the bias asymmetry between the two contact sections, with a spectral mismatch of up to 14 nm. Numerical simulations confirmed a relationship between this spectral asymmetry and the non-uniform filling of the quantum dots' confined states when different current densities are applied to the device electrodes. The results from this investigation open up an additional degree of freedom for multi-section superluminescent diodes, which could pave the way for optical bandwidth engineering via multiplexing the spectral output from both facets, using only a single device.

Published by The Optical Society under the terms of the Creative Commons Attribution 4.0 License. Further distribution of this work must maintain attribution to the author(s) and the published article's title, journal citation, and DOI.

1. Introduction

Superluminescent diodes (SLDs) have been shown to be key sources for a range of applications, including high-speed spectroscopy [1], metrology [2] and biological imaging using optical coherence tomography (OCT) [3]. While some applications, such as OCT, call for very large spectral bandwidths, there are other applications, for example in spectroscopy, where a high spectral brightness is more desirable [1]. As a result, there has been recent work regarding SLDs with moderate bandwidth but high spectral brightness [4,5] that could be low-cost and simple alternatives to supercontinuum sources in such applications [6]. In order to extend SLDs' spectral bandwidth and output power, and thus enhance their applicability, a number of approaches have been exploited. One example is spectral multiplexing, which couples two or more independent SLDs into a single output fibre to produce very wide optical spectra [3]. Multiplexing allows two or more SLDs to be operated far from their lasing limit and have their power and bandwidth summed, rather than driving a single device with very high current values. This technique has advantages associated with the independent biasing of distinct devices at the expense of increased complexity, cost and footprint. On the other hand, implementing multiple electrically-isolated contact sections in a single SLD has been shown as an alternative approach, where the optical power and spectrum can be optimized by independently tuning the current density in each section. Numerical simulations [7] and experimental work have shown the advantages of a multi-section contact approach in both narrow ridge [8,9] and tapered SLDs [10]. However, previous reports have only explored the output from one of the facets of the SLDs, with the exception of [11] and

#377768 https://doi.org/10.1364/OE.377768
Journal © 2020 Received 12 Sep 2019; revised 13 Dec 2019; accepted 16 Dec 2019; published 6 Jan 2020

Optics EXPRESS

[12]. In [11] the authors acquired a single spectrum from each facet of a quantum-well based SLD monolithically integrated with a tapered amplifier. This was carried out at a particular set of bias conditions, whereby the spectrum was taken from one facet while the opposite section was left unpumped, which fulfilled the research objective of the study but did not correspond to the common operating conditions of a wholly biased device. In these specific circumstances, the authors found the two spectra to be relatively similar. In [12], the authors demonstrated a QD device that underwent a selective area post growth annealing process to produce two spatially distinct regions where different proximity caps were used during the annealing process. The device was driven through a single electrical contact and a comparison between a single spectrum acquired from each facet was made. Again, although this satisfied the aims of the study, the results did not correspond to common SLDs which tend to have a uniformly processed active region. Spectral asymmetry between two outputs has been previously investigated in the context of lasers, such as reported in [13].

Here we present for the first time, a comparative investigation of the outputs from both facets of a multi-section SLD, which reveal a wide spectral asymmetry which was tunable with current density. Numerical simulations are able to reproduce these results considering a non-uniform carrier filling of the QDs' states in each section. This spectral asymmetry is an untapped degree of freedom which could be exploited for spectral bandwidth optimization via multiplexing from a single device. The work reported here also has wider implications for the simulation and experimental investigation of multi-section SLDs, optical amplifiers and external cavity lasers deploying such devices [14,15].

2. Experimental details

The active region of the SLD that was used contained 10 non-identical layers of InAs QDs that were capped by $In_{0.15}Ga_{0.85}As$ layers of variable thickness, comprising three QD layers grown for a central emission at 1211 nm, three QD layers at 1243 nm and four QD layers at 1285 nm (listed from the p-doped side to the n-side). The QD layers were separated by GaAs barriers with a 33 nm thickness. The SLD had a total length of 6 mm and consisted of three distinct geometrical segments [4]. At the rear of the device was a short, straight segment with a length of 0.5 mm and a ridge width of 14 µm. Following on from this was the first of two tapered segments, which also had a length of 0.5 mm and a taper angle of 1.5°. The final segment had a smaller taper angle of just 0.4° along the remaining 5 mm of the device length resulting in a front facet width of 110 µm. The three-segment geometry of the SLD waveguide was derived through simulations similar to those reported in [16], which were performed in order to simultaneously optimize the gain and beam quality emitted from the tapered facet of the device through manipulation of the waveguide design. This manipulation encompassed the inclusion of a shallow ridge at the waveguide border to introduce a weak index guiding to improve optical confinement.

An isolation trench was located 1.875 mm from the rear facet of the device meaning that the straight, first tapered and part of the second tapered segments (referred to as the rear section) were pumped through the rear contact and the remainder of the device (referred to as the front section) was pumped through the front contact. The front and rear sections had a contact area of 3.3×10^{-3} cm^2 and 6×10^{-4} cm^2 respectively, meaning that in order to achieve a constant current density across the whole device the rear section current would have to be 5.5 times smaller than the front section current. To achieve the lowest facet reflectivity possible, the device was tilted by 7° with respect to its facets and an anti-reflective coating was deposited. Throughout this investigation the SLD was driven with CW current sources through both its contacts and was maintained at a constant temperature of 20°C.

Optics EXPRESS

3. Results

3.1. Experimental

Light-current characteristics acquired from the rear facet of the SLD are shown in Fig. 1(a) alongside a plot of the rear facet power divided by the front facet power as a function of driving current, Fig. 1(b). These plots show that the output power from the rear facet was significant and potentially useful in its own right, with maximum powers of around 50 mW being achieved at combinations of high front and rear section current. The maximum output power emitted from the front facet of the SLD, as reported previously, was 137.5 mW at a front section current of 4 A and a rear section current of 0.7 A [4]. The corresponding rear facet output power under these biasing conditions was 48.5 mW, resulting in a total combined output power from the SLD of 186 mW. It is worth noting that this potential 35% boost to the output power comes at little to no cost to the spectral bandwidth, unlike conventional increases in output power which are achieved through increasing the driving current and often lead to a narrowing of the optical spectrum. This could also further enhance the spectral brightness of the SLD.

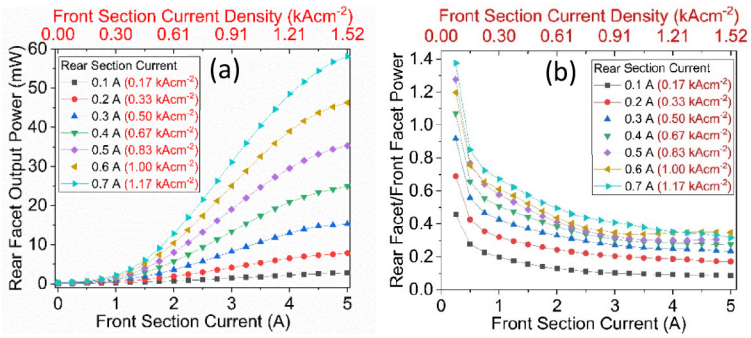

Fig. 1. (a) Light-current characteristics output from rear facet. (b) Rear facet output power divided by front facet output power vs front section current. Rear section current densities are indicated with red text in the legend of both plots.

Contributions from rear facet emission to the combined total output power of the SLD were found to not only improve the device performance in the high driving current regime but also have a meaningful impact at low driving currents. The two section contact layout of the SLD allowed for a large degree of tunability in the front facet spectral bandwidth and output power. Indeed, at low front section currents of 1 A and rear section currents of 0.1–0.4 A, front facet spectral bandwidths of around 75 nm were attained at low output powers of around 2 mW. As can be seen from Fig. 1(b), the rear facet output power as a fraction of the front facet power was highest at low front section currents and tended to decrease as front section current was increased. This means that proportionately, the largest boosts to the total combined output power of the SLD from rear facet contributions were possible at low front section driving currents, where the highest bandwidths were observed. As an example, at 1 A and 0.4 A of front and rear section current respectively, where the front facet spectral bandwidth was 73 nm, the total combined output power was 3.5 mW, a 50% improvement over the original front facet power of 2.3 mW.

While maintaining a fixed rear section current of 0.1 A, optical spectra were acquired from both facets for increasing front section current. As shown in Fig. 2, a comparison between the output from both facets revealed an increasing asymmetry with increasing front section current, which manifested mainly as a blue-shifting front facet spectra relative to fairly consistent rear facet spectra. This was likely due to the fact that in Fig. 2, the front section current was changing while the rear section current remained fixed. This spectral asymmetry was a reflection of both the asymmetry of the tapered waveguide and the inhomogeneous pumping of the two sections

Optics EXPRESS

of the SLD. In addition to the important role that the tapered geometry of the SLD waveguide has in boosting the output power, one also has to consider the fact that light is generated within the waveguide propagating in all directions, which results in coupled but different dynamics in each of the sections of the SLD which are dependent on the direction of propagation through the device.

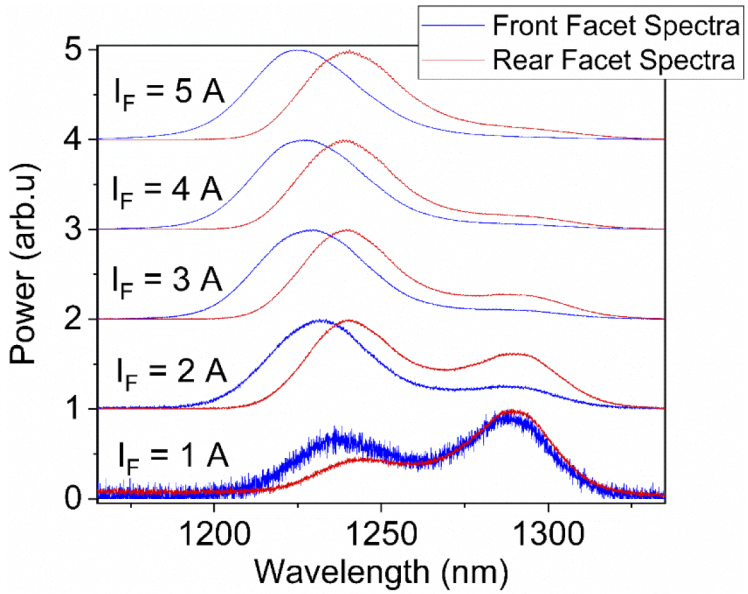

Fig. 2. Front and rear facet optical spectra at a fixed rear section current of 0.1 A. The normalized spectra are shifted vertically for illustration purposes.

The spectral asymmetry can be further enhanced and controlled through the bias conditions applied to each contact section, as current density variations lead to changes in the gain saturation, quantum-dot state filling and junction temperature. Indeed, through exploring the range of bias applied to both sections, it became apparent that the asymmetry in current densities applied to both sections was a key driving factor in extending the spectral asymmetry. Confining the analysis to the spectral feature around 1235 nm which is present in the spectra of both facets, the trend of central wavelength showed how spectral mismatch generally increased with asymmetry in bias conditions. This is illustrated in Fig. 3, where the difference in the central wavelength of the front and rear facet spectra is plotted as a function of the front and rear section driving current density, Fig. 3(a). Also shown is the center wavelength of the optical spectra emitted from the front and rear facet as a function of front and rear section current density in Figs. 3(b) and 3(c), respectively. The difference in center wavelength was calculated by subtracting the front facet center from the rear facet center wavelength. The difference in driving current densities was calculated by subtracting the rear section current density from the front section current density.

Generally, for a fixed front section current density, as the magnitude of the difference in current density between the two sections of the SLD increased, the central wavelength difference, and hence the spectral asymmetry, between the front and rear facet spectra also tended to increase. A maximum central wavelength difference of 14 nm was observed at the maximum measured current density difference of 1.35 kAcm^{-2}, which corresponded to rear/front current densities of 0.17/1.52 kAcm^{-2}. However, it is also clear from Fig. 3(a) that the front/rear facet spectral asymmetry was not solely dependent on the magnitude of the difference in current density between the two sections. This is evidenced by the fact that very similar differences in driving

Optics EXPRESS

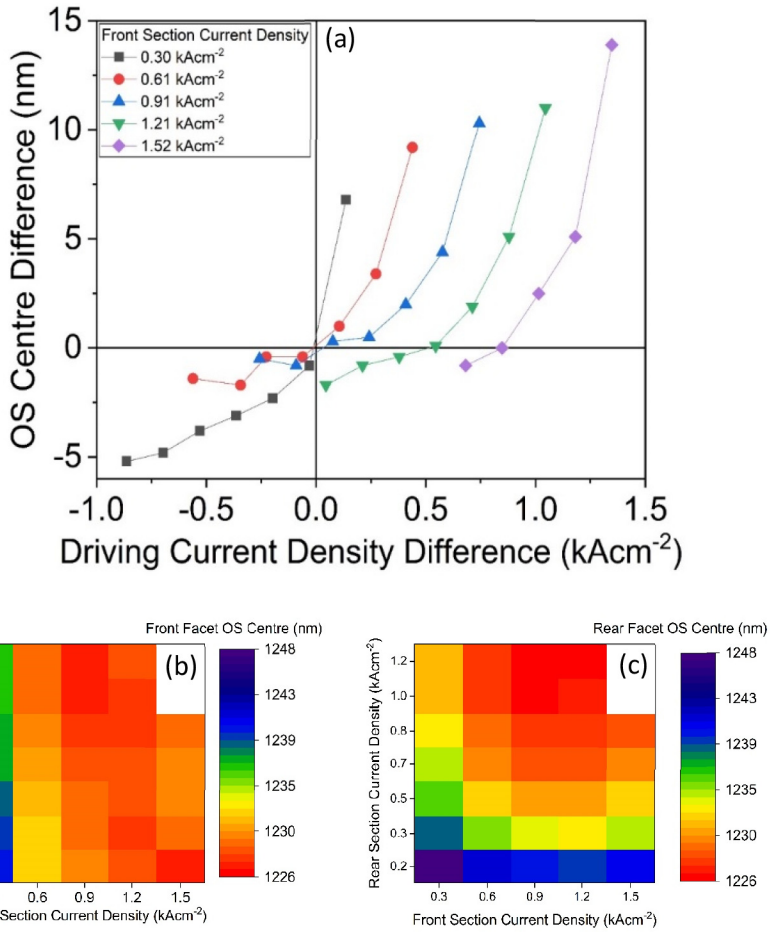

Fig. 3. (a) Plot of the difference in the front and rear facet optical spectra (OS) central peak wavelength vs the difference in the driving current densities applied to the front and rear sections. (b) and (c) front and rear facet optical spectra central wavelengths vs front and rear section current density (confining the analysis to the spectral feature around 1235 nm which is present in the spectra of both facets).

current density resulted in significantly different magnitudes of spectral asymmetry, depending on the specific front and rear section current densities that were applied. This was likely due to the fact that the gain spectra in each section of the device were also dependent on the absolute values of current density applied. Therefore, the same difference in current density values between the two sections of the SLD could result in different gain spectra in each section and hence different magnitudes of front/rear facet spectral asymmetry.

3.2. Numerical simulations

In order to better understand the origin of the reported strong spectral asymmetry, we use a rate-equation based QD model taking into account the multilayer chirped active material, the spatial distribution of the QD carriers and the spectral and spatial distribution of the photons in the SLD. The model is developed starting from the one originally presented in [17].

Optics EXPRESS

We consider a system formed by n_l QD layers with a fundamental confined state (ground state, GS) and two excited states (ES_1, ES_2) having degeneracy μ_i ($i = GS, ES_1, ES_2$); a quasi-2D wetting layer (WL) is also included.

In each layer l of active material, we supposed that the occupation probability in the confined states of each single QD does not depend on its size. While the distribution of carriers in each layer may depend on both the longitudinal (z) and lateral directions, we consider in the following only the variation in the longitudinal direction in order to reduce the computational effort of the numerical solution. Finally, we use an excitonic approach, i.e. we assume that the occupation of the holes in valence band and electrons in conduction band have the same occupation probability. With these assumptions, we indicate with $\rho_i^l(z)$ the spatially dependent occupation probability in the three considered confined states ($i = GS, ES_1, ES_2$) for the dots in layer l.

Each confined state is associated to a transition energy E_i^l, while all the WLs share the same transition energy E_{WL}. We indicate as $\Delta E^l_{WL-ES_2} = \delta^e(E_{WL} - E^l_{ES_2})$, $\Delta E^l_{ES_2-ES_1} = \delta^e(E^l_{ES_2} - E^l_{ES_1})$, and $\Delta E^l_{ES_1-GS} = \delta^e(E^l_{ES_1} - E^l_{GS})$ the interband transition energies between couples of adjacent energy states, with $\delta^e = 80$.

The gain (per meter) and the spontaneous emission rate (per electron-Volt and per second) of each QD layer l are both functions of energy E and can be written as the sum of gain $g_i^l(z, E)$ and spontaneous emission rate $R^l_{sp,i}(z, E)$ of each confined state:

$$g^l(z, E) = \sum_{i=GS,ES_1,ES_2} g_i^l(z, E) \sum_{i=GS,ES_1,ES_2} \mu_i A(E_i^l) G(E - E_i^l)(2\rho_i^l(z) - 1) \tag{1}$$

$$\begin{aligned} R^l_{sp}(z, E) &= \sum_{i=GS,ES_1,ES_2} R^l_{sp,i}(z, E) \\ &= \sum_{i=GS,ES_1,ES_2} \mu_i \frac{n^2}{\pi^2 c^2 \hbar^2} (E_i^l)^2 A(E_i^l) V_{QD} G(E - E_i^l) \rho_i^l(z)^2 \end{aligned} \tag{2}$$

with n effective refractive index, c speed of light, $\hbar$ normalized Planck constant, and V_{QD} volume of a single QD. In Eq. (1) and Eq. (2), the term A contains the interband transition matrix element; for each confined state $i = GS, ES_1, ES_2$, the variation of A with respect to energy is weak, and we assume that $A(E_i^l) = A(E_i) = A_i$. Finally, $G(E)$ is a Gaussian distribution used to model the QD inhomogeneous broadening; it has Full-Width at Half Maximum ΔE_{FWHM} and its peak value, around E_i^l, is $G_{\max} = 2\sqrt{\log 2}/\sqrt{\pi}\Delta E_{FWHM}$. The product $A(E_i)G_{\max} = g_i$ is the maximum gain (per unit length) of the confined state i.

The allowed transitions among the considered confined states are shown, for a generic QD layer, in Fig. 4, where carrier capture and escape rates are described through characteristic times τ_c and τ_e^l and take into account Pauli blocking terms. The Auger recombination rates are introduced in the rate equations using a cubic dependence on the carrier occupation probabilities [18]; they are associated with characteristic times $\tau_{A,j}$ while non-radiative recombinations are included with time constants $\tau_{nr,j}$ ($j = GS, ES_1, ES_2, WL$). We assume that each QD layer receives a fraction $I(z)/n_l$ of the externally applied current $I(z)$; such a fraction is injected directly in the WL. This hypothesis is valid if carrier transport effects across the barriers can be neglected.

The resulting system of rate equations reads:

$$\frac{dN^l_{WL}(z)}{dt} = \zeta_{ES_2} \frac{\rho^l_{ES_2}}{\tau^l_{e,ES_2}} - \frac{N^l_{WL}(1 - \rho^l_{ES_2})}{\tau_{c,WL}} - \frac{N^l_{WL}}{\tau_{nr,WL}} + \frac{\eta I}{e n_l V_{WL}} = 0 \tag{3}$$

Optics EXPRESS

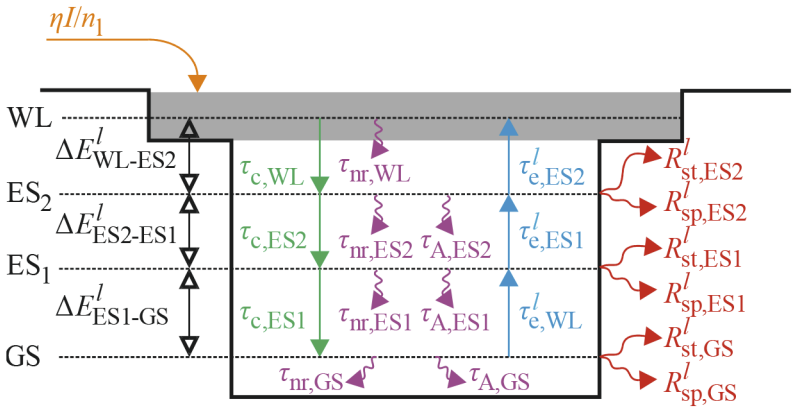

Fig. 4. Schematic representation of the energy levels of layer l. The pumping term (orange), the capture (green) and escape (blue) transitions, the non-radiative and Auger recombinations (purple), and the stimulated and spontaneous emission (red) are indicated by arrows.

$$\frac{\mathrm{d}\rho^l_{\text{ES}_2}(z)}{\mathrm{d}t} = -\frac{\rho^l_{\text{ES}_2}}{\tau^l_{\text{e,ES}_2}} + \frac{1}{\zeta_{\text{ES}_2}}\frac{N^l_{\text{WL}}}{\tau_{\text{c,WL}}} + \frac{\mu_{\text{ES}_1}}{\mu_{\text{ES}_2}}\frac{\rho^l_{\text{ES1}}(1-\rho^l_{\text{ES}_2})}{\tau^l_{\text{e,ES}_1}} - \frac{\rho^l_{\text{ES}_2}(1-\rho^l_{\text{ES}_1})}{\tau_{\text{c,ES}_2}} - \frac{N^l_{\text{ES}_2}}{\tau_{\text{nr,ES}_2}} - \frac{(\rho^l_{\text{ES}_2})^3}{\tau_{\text{A,ES}_2}} - R^l_{\text{sp,ES}_2} - R^l_{\text{st,ES}_2} = 0 \tag{4}$$

$$\frac{d\rho^l_{ES_1}(z)}{dt} = -\frac{\rho^l_{\text{ES}_1}(1-\rho^l_{\text{ES}_2})}{\tau^l_{\text{e,ES}_1}} + \frac{\mu_{\text{ES}_2}}{\mu_{\text{ES}_1}}\frac{\rho^l_{\text{ES}_2}(1-\rho^l_{\text{ES}_1})}{\tau_{\text{c,ES}_2}} + \frac{\mu_{\text{GS}}}{\mu_{\text{ES}_1}}\frac{\rho^l_{\text{GS}}(1-\rho^l_{\text{ES}_1})}{\tau^l_{\text{e,GS}}} - \frac{\rho^l_{\text{ES}_1}(1-\rho^l_{\text{GS}})}{\tau_{\text{c,ES}_1}} - \frac{N^l_{\text{ES}_1}}{\tau_{\text{nr,ES}_1}} - \frac{(\rho^l_{\text{ES}_1})^3}{\tau_{\text{A,ES}_1}} - R^l_{\text{sp,ES}_1} - R^l_{\text{st,ES}_1} = 0 \tag{5}$$

$$\frac{\mathrm{d}\rho^l_{\text{GS}}(z)}{\mathrm{d}t} = -\frac{\rho^l_{\text{GS1}}(1-\rho^l_{\text{ES}_1})}{\tau^l_{\text{e,GS}}} + \frac{\mu_{\text{ES}_1}}{\mu_{\text{GS}}}\frac{\rho^l_{\text{ES}_1}(1-\rho^l_{\text{GS}})}{\tau_{\text{c,ES}_1}} - \frac{(\rho^l_{\text{GS}})^3}{\tau_{\text{A,GS}}} - \frac{N^l_{\text{GS}}}{\tau_{\text{nr,GS}}} - R^l_{\text{sp,GS}} - R^l_{\text{st,GS}} = 0 \tag{6}$$

where N^l_{WL} is the carrier density in the WL of layer l, η is the injection efficiency, V_{WL} is the layer volume, and e indicates the electron charge. The term $\zeta_i = \mu_i N_\text{d}/h_{\text{WL}}$ allows to convert the occupation probability of confined state i into the corresponding carrier density, with N_d denoting the QD density per unit area and h_{WL} the height of a QD layer. The terms R^l_{st} describe the stimulated emission processes occurring in the confined states, respectively, and will be derived in the following. The escape rates appearing in Eqs. (3)–(6) are related to the capture rate in a quasi-equilibrium approximation [19]:

$$\tau_{\text{e,ES}_2} = \tau_{\text{c,WL}}\frac{\mu_{\text{ES}_2}\pi\hbar^2}{m^*_\text{e}k_\text{B}T}N_\text{d}e^{\frac{\Delta E^l_{WL-\text{ES}_2}}{k_BT}} \tag{7}$$

$$\tau_{\text{e,(ES}_1\text{,GS)}} = \tau_{\text{c,(ES}_2\text{,ES}_1)}\frac{\mu_{(\text{ES}_1,\text{GS})}}{\mu_{(\text{ES}_2,\text{ES}_1)}}e^{\frac{\Delta E^l_{(\text{ES}_2-\text{ES}_1,\text{ES}_1-\text{GS})}}{k_BT}}. \tag{8}$$

In order to accurately introduce the interaction between carriers and photons in the SLD waveguide, the portion of interest of the optical spectrum is divided into M uniformly distributed intervals, centered around energy E_m and with amplitude $2\Delta E$, so that $S^\pm_m(z)$ ($m \in [1, M]$) is the number of

Optics EXPRESS

photons with energy in the range $(E_m - \Delta E, E_m + \Delta E)$ propagating in the $+z$ and $-z$ directions, respectively.

The spatial evolution of $S_m^{\pm}(z)$ is described, for each portion m of the spectrum, by means of differential equations:

$$\pm\frac{\mathrm{d}S_m^{\pm}(z)}{\mathrm{d}z} = \frac{\beta_{sp}}{2v_g}R_{sp,m}(z) + (\Gamma^{\pm}(z)g_m(z) - \alpha_i^{\pm} - \alpha_p(z))S_m^{\pm}(z) \tag{9}$$

with v_g group velocity, β_{sp} spontaneous emission coefficient, $\alpha_p(z)$ plasma induced losses, proportional to the total WL carriers; the boundary conditions in $z = 0$ and $z = L$ read $S_m^+(0) = R_0 S_m^-(0)$ and $S_m^-(L) = R_L S_m^+(L)$, with R_0 and R_L residual reflectivities at the SLD end facets.

In gain guided tapered SLDs, the generally weak confinement of the electric field could result in different values of the transverse confinement factor and propagation losses; in particular, the field observing a narrowing of the waveguide width typically observes larger losses and smaller confinement factors due to the refocusing capability of the gain guiding mechanism. This effect is introduced in the model through the direction-dependent terms $\Gamma^{\pm}(z)$ and $\alpha_i^{\pm}$, which can be estimated, e.g., using Beam Propagation Methods simulations taking into account the QD nature of the active material [16,20].

In Eq. (9), the gain g_m is the result of the sum of the contributions from all the n_l QD layers:

$$g_m(z) = \sum_{l=1}^{n_l} g^l(E_m) \tag{10}$$

and the term $R_{sp,m}(z)$ is the rate of spontaneous emission coupled into $S_m^{\pm}(z)$ and is given by the integral of the energy dependent spontaneous emission rate calculated in Eq. (2), summed over all the QD layers:

$$R_{\mathrm{sp},m}(z) = \int_{E_m-\Delta E}^{E_m+\Delta E} \sum_{l=1}^{n_l} R_{\mathrm{sp}}^l(z,E)\mathrm{d}E. \tag{11}$$

Finally, the stimulated emission terms appearing in Eqs. (3)–(6) can be written considering the interaction of photons $S^{\pm}(z, E_m)$ with the population i thanks to the inhomogeneous broadening of its emission:

$$\begin{gathered} R_{\mathrm{st},i}^l(z) = -v_g\mu_i N_{\mathrm{d}}\frac{\Gamma^+ + \Gamma^-}{2}A_i\frac{V_{QD}}{h_{\mathrm{QD}}}(2\rho_i^l(z) - 1) \\ \sum_{m=1}^{M} G(E_m - E_i^l)(S^+(z,E_m) + S^-(z,E_m)), \quad i = \mathrm{GS}, \mathrm{ES1}, \mathrm{ES2}. \end{gathered} \tag{12}$$

For the numerical solution of the system of coupled Eqs. (3)–(6) and (9), the SLD is uniformly discretized in the z direction; differential equations are integrated in space using a finite difference scheme. Following the approach proposed in [17], in order to speed up the calculation of a self-consistent solution for carriers and photons, a two-step method is used, which proved, for this application, to be advantageous with respect to other numerical methods more commonly used. First, the distribution of carriers is calculated in the absence of photons. This solution constitutes the initial guess of an iterative method which solves for the spatial distribution of photons (Eq. (9)) assuming the carrier distribution is known and then uses this result to calculate the filling of the QD states (Eqs. (3)–(6)), until convergence is reached.

The physical parameters used in the simulation of the considered 6 mm long SLD are listed in Table 1. The resulting density of states of the complete QD ensemble, taking into account the chirped nature of the considered active material, is shown in Fig. 5, where the overlap is clearly visible between the different QD allowed transition energies thanks to the chirping of the QD layers and to the inhomogeneous broadening.

Optics EXPRESS

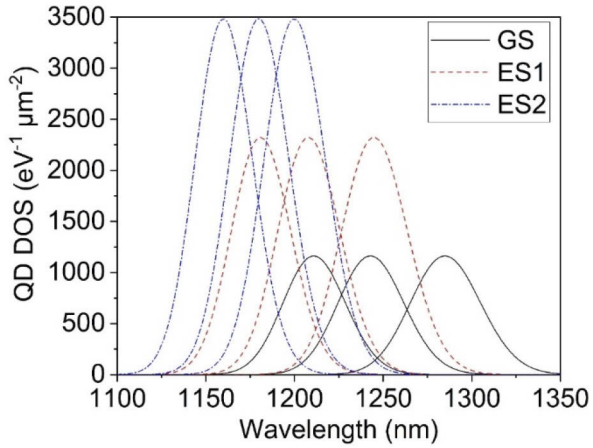

Fig. 5. Density of states of the considered chirped QD material.

Table 1. Physical parameters used in the numerical simulations

Symbol	Meaning	Value
η	Injection efficiency	0.65
n_l	Number of QD layers	4 + 3 + 3
E^l_{GS}	GS transition energies	1.0239–0.9976–0.9650 eV
E^l_{ES1}	$\mathrm{ES_1}$ transition energies	1.0500–1.0265–0.9960 eV
E^l_{ES1}	$\mathrm{ES_2}$ transition energies	1.0690–1.0508–1.0333 eV
E_{WL}	WL transition energy	1.1 eV
ΔE_{FWHM}	FWHM inhomo. broad.	35 meV
N_{d}	QD surface density	400 cm^{-2}
g_{i}	GS, $\mathrm{ES_1}$, $\mathrm{ES_2}$ maximum gain	690–750 – 700 cm^{-1}
$\alpha^{\pm}$	Propagation losses	1.35 (+), 3.60(-) cm^{-1}
K_{p}	Plasma losses coefficient	10^{-17} cm^2
$\tau_{\mathrm{c},i}$	Capture times from $\mathrm{ES_1}$, $\mathrm{ES_2}$, WL	5–5 – 12 ps
$\tau_{\mathrm{nr},i}$	Non-radiative times for GS, $\mathrm{ES_1}$, $\mathrm{ES_2}$, WL	10 ns
$\tau_{\mathrm{A},i}$	Auger times from GS, $\mathrm{ES_1}$, $\mathrm{ES_2}$	0.44–2.2 –3.3 ns
h_{WL}	WL height	8 nm

The first objective of the analysis was to reproduce the light-current characteristic measured at the device facets in a condition of uniform current injection. The results are shown, in linear and logarithmic scale, in Fig. 6. Numerical and experimental results are in good agreement, in particular for current densities above 0.4 kAcm^{-2}. It is worth pointing out that below this value of injection the SLD power is 0 dBm or less, and therefore of limited interest for practical applications.

Under a non-uniform current injection, the numerical simulations reproduce the interesting evolution in the optical spectra experimentally observed and reported in Fig. 2. In particular, Fig. 7 shows the results obtained for a rear section current of 0.1 A and a front section current of 1 A. For this particular choice of the injected currents, the simulated optical spectra are in qualitative agreement with the experimental findings, where the two spectra share the same shape and present maxima for similar wavelengths, Fig. 7(a). The QD occupation probabilities close to

Optics EXPRESS

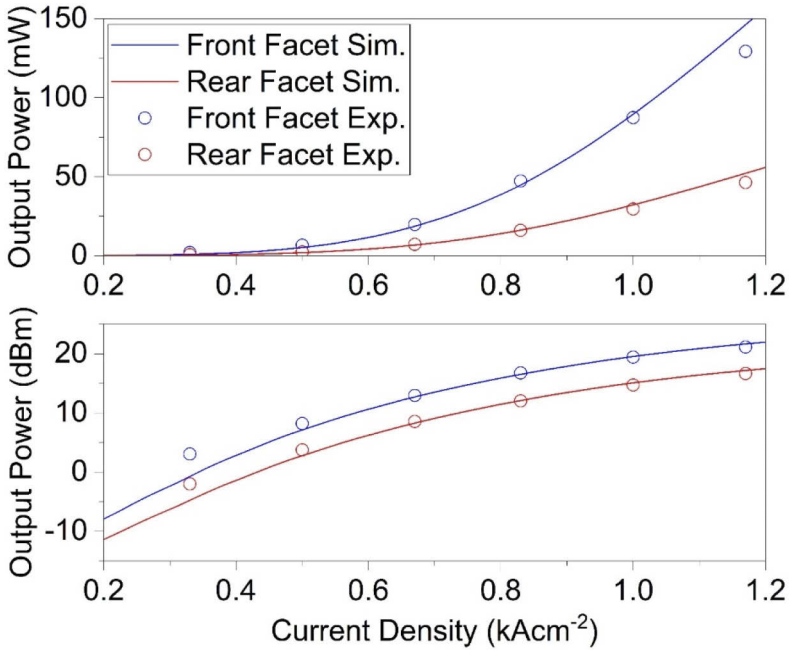

Fig. 6. Comparison of simulated (continuous lines) and experimental (markers) powers at the front (blue) and rear (red) facets of the considered SLD, in linear (top) and logarithmic (bottom) scales.

the front facet, Fig. 7(b) and to the rear facet, Fig. 7(c), are also similar. It is worth observing that the occupation probabilities are higher for the groups of QD with GS energy at 1285 nm than for the other QD groups, due to the slower escape rates of the former. Because of the relatively low injected current densities, only the ground states are able to provide optical amplification while the excited states are absorbing, and the field propagating in the device can experience a positive net modal gain only between 1225 nm and 1300 nm, approximately. Finally, Fig. 7(e) shows the spatial distribution of forward (continuous line) and backward (dashed line) propagating photons at 1250 nm (green) and 1275 nm (magenta).

As in the experiment, a different operating condition, with asymmetric output spectra, can be reproduced when a higher current is applied to the front section. Figure 8 focuses on the case of a rear section current of 0.1 A and a front section current of 3.5 A. In these conditions, the simulated optical spectrum at the front facet presents a maximum at approximately 1210 nm, while the spectrum at the rear facet presents a maximum around 1240 nm, Fig. 4(a). Due to the strongly non-uniform current injection, the occupation probabilities close to the two SLD facets are now different. At the front facet, Fig. 8(b), only the second excited states associated to QD with GS at 1210 nm are still absorbing; the corresponding net modal gain Fig. 8(d), blue curve) is now blue shifted with respect to the case in Fig. 7, with a maximum at 1210 nm. On the other hand, the current injected in the rear section is the same as in the previous considered case, and both occupation probabilities, Fig. 8(c), and net modal gain (Fig. 8(d), red curve) close to the rear facet are similar to the ones reported in Fig. 7, with only the ground states above transparency.

Observing the photons propagating in the forward direction, these are spontaneously generated and amplified at 1210 nm (green lines in Fig. 8) and at 1240 nm (magenta lines) in the front section only, since the rear section is absorbing at those wavelengths. The gain at 1210 nm is larger and so the output spectrum therefore has a peak at this wavelength. Photons propagating in the backward direction are generated and amplified in the front section, and are absorbed in

Optics EXPRESS

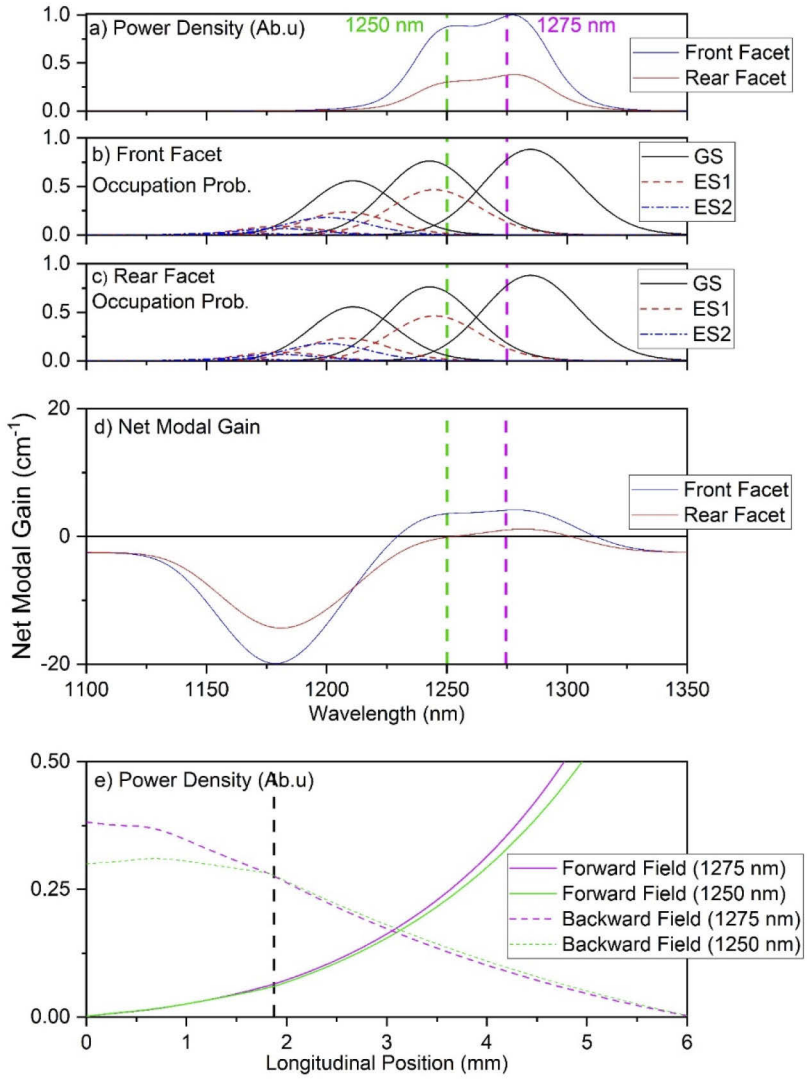

Fig. 7. Simulation results for a non-uniform current injection (rear section: 0.1 A, front section: 1 A). (a) Output optical spectra at the front (blue) and rear (red) facets. (b) occupation probabilities close to the front facet. (c) occupation probabilities close to the rear facet. (d) net modal gain. (e) evolution of the number of photons propagating in the forward (continuous line) and backward (dashed line) directions at 1250 nm (green) and 1275 nm (magenta). Dashed black line separates the rear and front sections. The maximum of the green curve is normalized to 1.

Optics EXPRESS

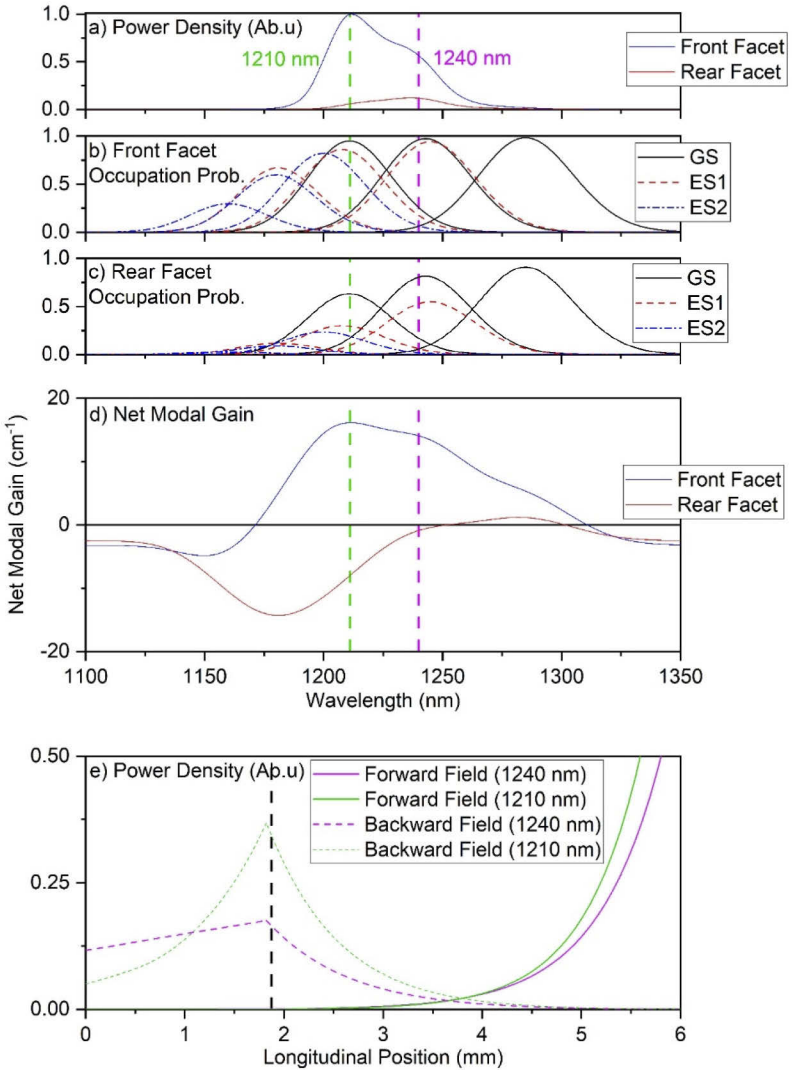

Fig. 8. Simulation results for a non-uniform current injection (rear section: 0.1 A, front section: 3.5 A). (a) Output optical spectra at the front (blue) and rear (red) facets. (b) occupation probabilities close to the front facet. (c) occupation probabilities close to the rear facet. (d) net modal gain. (e) evolution of the number of photons propagating in the forward (continuous line) and backward (dashed line) directions at 1210 nm (green) and 1240 nm (magenta). Dashed black line separates the rear and front sections. The maximum of the green curve is normalized to 1.

the rear one. The absorption at 1210 nm is much stronger than at 1240 nm and, as a result, the spectrum at the rear facet presents a peak around 1240 nm.

These numerical simulations have given an insight into the mechanisms responsible for the asymmetry in both the output power and optical spectra that was observed from the two facets of the SLD. Furthermore, they point towards the design factors that could affect both the power and spectral asymmetries with the QD layers chirp and the ratio between the front and rear sections contact areas being the main parameters to control.

Optics EXPRESS

4. Conclusion and outlook

In summary, for the first time we present a comparative investigation of the outputs from both facets of an SLD. Observation of the optical spectra from the front and rear facets of a two section, tapered SLD under various biasing conditions revealed a spectral asymmetry between the outputs which was highly dependent on the mismatch in the current densities applied to the two sections of the device. This asymmetry, as characterized by the difference in the central wavelengths of the front and rear facet spectra, grew to be as large as 14 nm at 0.17/1.52 kAcm^{-2} of rear/front section driving current density. Measurement of the output power from the rear facet showed that not only could this output be useful in its own right, with a maximum output power of 50 mW, but also that through multiplexing, the maximum total combined output power from the SLD could be boosted by 35% to 186 mW (20 nm spectral bandwidth) with little to no cost to spectral bandwidth. Numerical simulations taking into account the properties of the chirped QD active material and the optical properties of the tapered gain guided waveguide reproduced the experimental findings and explained the asymmetry in the optical spectra at the SLD facets in terms of different filling of the confined QD states in the two non-uniformly pumped regions.

Comparison and utilization of the output from both facets of an SLD represents a new avenue of device design that could be exploited to optimize the output from a single device. The flexibility afforded by this approach could also allow one to access different regimes of operation from a single device and/or targeting different subsets of applications with different requirements in terms of spectral bandwidth, central wavelength or optical power, as the rear facet output could be virtually used as a separate SLD. Alternatively, combining both outputs could provide a means to enhance the bandwidth and power using multiplexing with a single device. In order to broaden the versatility of this approach, future devices could be designed to have additional and/or shorter sections, where the bias imbalance between them could be enhanced, thus leading to a greater spectral asymmetry, potentially exploiting different populations of QDs and/or states (ground/excited). Further consideration could also be given to the respective position of each QD layer within a chirped active region, relative to the p-contact, in order to affect the carrier density in each layer and hence manipulate the output spectrum. Moreover, additional spectral shaping (such as with frequency selective optical feedback [21]) involving the asymmetric outputs of both facets could provide a route to control and extend the spectral bandwidth even further. Such an approach would have significant advantages in terms of cost, size, complexity and power consumption, compared with traditional multi-source multiplexing.

Moreover, the results presented here show that spectral asymmetry between the outputs from different facets is an aspect that merits consideration in further simulation and experimental studies of multi-section SLDs, optical amplifiers and external-cavity lasers deploying such devices. Such spectral asymmetry represents an additional degree of freedom which has remained untapped so far and its exploitation could lead to a new generation of semiconductor devices with enhanced functionalities.

Funding

H2020 European Research Council (640537); FP7 Information and Communication Technologies (224338); Engineering and Physical Sciences Research Council; Biotechnology and Biological Sciences Research Council.

Acknowledgments

The authors would like to thank Innolume GmbH (Germany) for the growth of the QD wafers. The authors would like to thank T. Xu, M. Rossetti and I. Montrosset for stimulating discussions. From III-V Lab the authors would also like to thank M. Tran for SLD processing, Y. Robert for

Optics EXPRESS

the SLD low-reflectivity coating, E. Vinet and M. Garcia for SLD mounting and M. Ruiz for characterization. Supporting data is available at https://researchportal.hw.ac.uk/.

References

1. W. Denzer, M. L. Hamilton, G. Hancock, M. Islam, C. E. Langley, R. Peverall, and G. A. D. Ritchie, "Near-infrared broad-band cavity enhanced absorption spectroscopy using a superluminescent light emitting diode," Analyst **134**(11), 2220–2223 (2009).
2. S. Lawman and H. Liang, "High precision dynamic multi-interface profilometry with optical coherence tomography," Appl. Opt. **50**(32), 6039–6048 (2011).
3. T. H. Ko, D. C. Adler, J. G. Fujimoto, D. Mamedov, V. Prokhorov, V. Shidlovski, and S. Yakubovich, "Ultrahigh resolution optical coherence tomography imaging with a broadband superluminescent diode light source," Opt. Express **12**(10), 2112–2119 (2004).
4. A. F. Forrest, M. Krakowski, P. Bardella, and M. A. Cataluna, "High-power quantum-dot superluminescent tapered diode under CW operation," Opt. Express **27**(8), 10981–10990 (2019).
5. A. T. Aho, J. Viheriälä, H. Virtanen, N. Zia, R. Isoaho, and M. Guina, "High power GaInNAs superluminescent diodes emitting over 400 mW in the 1.2 µm wavelength range," Appl. Phys. Lett. **115**(8), 081104 (2019).
6. A. Aalto, G. Genty, T. Laurila, and J. Toivonen, "Incoherent broadband cavity enhanced absorption spectroscopy using supercontinuum and superluminescent diode sources," Opt. Express **23**(19), 25225–25234 (2015).
7. M. Rossetti, P. Bardella, and I. Montrosset, "Numerical investigation of power tunability in two-section QD superluminescent diodes," Opt. Quantum Electron. **40**(14–15), 1129–1134 (2008).
8. Y. C. Xin, A. Martinez, T. Saiz, A. J. Moscho, Y. Li, T. A. Nilsen, A. L. Gray, and L. F. Lester, "1.3-µm Quantum-Dot Multisection Superluminescent Diodes With Extremely Broad Bandwidth," IEEE Photonics Technol. Lett. **19**(7), 501–503 (2007).
9. P. D. L. Greenwood, D. T. D. Childs, K. M. Groom, B. J. Stevens, M. Hopkinson, and R. A. Hogg, "Tuning Superluminescent Diode Characteristics for Optical Coherence Tomography Systems by Utilizing a Multicontact Device Incorporating Wavelength-Modulated Quantum Dots," IEEE J. Sel. Top. Quantum Electron. **15**(3), 757–763 (2009).
10. X. Li, P. Jin, Q. An, Z. Wang, X. Lv, H. Wei, J. Wu, J. Wu, and Z. Wang, "Experimental investigation of wavelength-selective optical feedback for a high-power quantum dot superluminescent device with two-section structure," Opt. Express **20**(11), 11936–11943 (2012).
11. D. Guotong, G. Devane, K. A. Stair, W. Shengli, R. P. H. Chang, Z. Yongsheng, S. Zhongzhe, L. Ying, J. Xiuying, and H. Weihua, "The monolithic integration of a superluminescent diode with a power amplifier," IEEE Photonics Technol. Lett. **10**(1), 57–59 (1998).
12. Z. Y. Zhang, Q. Jiang, M. Hopkinson, and R. A. Hogg, "Effects of intermixing on modulation p-doped quantum dot superluminescent light emitting diodes," Opt. Express **18**(7), 7055–7063 (2010).
13. I. Stamataki, A. Kapsalis, S. Mikroulis, D. Syvridis, M. Hamacher, U. Troppenz, and H. Heidrich, "Modal properties of all-active InGaAsP/InP microring lasers," Opt. Commun. **282**(12), 2388–2393 (2009).
14. S. Haggett, M. Krakowski, I. Montrosset, and M. A. Cataluna, "High-power quantum-dot tapered tunable external-cavity lasers based on chirped and unchirped structures," Opt. Express **22**(19), 22854–22864 (2014).
15. S. E. White and M. A. Cataluna, "Unlocking Spectral Versatility from Broadly-Tunable Quantum-Dot Lasers," Photonics **2**(2), 719–744 (2015).
16. T. Xu, P. Bardella, M. Rossetti, and I. Montrosset, "Beam propagation method simulation and analysis of quantum dot flared semiconductor optical amplifiers in continuous wave high-saturation regime," IET Optoelectron. **6**(2), 110–116 (2012).
17. P. Bardella, M. Rossetti, and I. Montrosset, "Modeling of Broadband Chirped Quantum-Dot Super-Luminescent Diodes," IEEE J. Sel. Top. Quantum Electron. **15**(3), 785–791 (2009).
18. P. Blood, H. Pask, H. D. Summers, and I. Sandall, "Localized Auger Recombination in Quantum-Dot Lasers," IEEE J. Quantum Electron. **43**(12), 1140–1146 (2007).
19. M. Rossetti, L. Li, A. Markus, A. Fiore, L. Occhi, C. Velez, S. Mikhrin, I. Krestnikov, and A. Kovsh, "Characterization and Modeling of Broad Spectrum InAs–GaAs Quantum-Dot Superluminescent Diodes Emitting at 1.2–1.3µm," IEEE J. Quantum Electron. **43**(8), 676–686 (2007).
20. P. Bardella, L. Drzewietzki, M. Krakowski, I. Krestnikov, and S. Breuer, "Mode locking in a tapered two-section quantum dot laser: design and experiment," Opt. Lett. **43**(12), 2827–2830 (2018).
21. M. Blazek, W. Elsäßer, M. Hopkinson, P. Resneau, M. Krakowski, M. Rossetti, P. Bardella, M. Gioannini, and I. Montrosset, "Coherence function control of Quantum Dot Superluminescent Light Emitting Diodes by frequency selective optical feedback," Opt. Express **17**(16), 13365–13372 (2009).